Additive manufacturing of corrosion-resistant maraging steel M789 by directed energy deposition

Yung Zhen Lek [a b], Chengcheng Wang [a b], Xiaojun Shen [c], Ze Chen [a b], Upadrasta Ramamurty [b], Kun Zhou [a b]

[a] Singapore Centre for 3D Printing, School of Mechanical and Aerospace Engineering, Nanyang Technological University, 50 Nanyang Avenue, Singapore, 639798, Singapore

[b] School of Mechanical and Aerospace Engineering, Nanyang Technological University, 50 Nanyang Avenue, Singapore, 639798, Singapore

[c] School of Electrical and Electronic Engineering, Nanyang Technological University, 50 Nanyang Avenue, Singapore, 639798, Singapore

Abstract

Conventional maraging steels feature a combination of high strength and toughness, but they often suffer from low corrosion resistance. Hence, maraging steel M789 was developed to alleviate this issue while maintaining its strength. Most studies of maraging steels processed by additive manufacturing (AM) focus on utilizing laser powder bed fusion (LPBF). However, the research in laser-directed energy deposition (L-DED) fabrication of corrosion-resistant maraging steels is limited. The different cooling rates experienced by materials during L-DED and LPBF processing give rise to differing microstructures and mechanical properties. In this study, the L-DED process was adopted to manufacture nearly-fully dense M789 parts, which were subsequently subjected to direct aging and solutionizing + aging heat treatments. Electron backscatter diffraction (EBSD) analysis reveals a martensitic structure in both as-fabricated and heat-treated samples with the presence of austenite in the as-fabricated and directly aged samples. Scanning transmission electron microscopy (STEM) and transmission Kikuchi diffraction (TKD) reveal the presence of Ti- and Al-rich precipitates within the martensites after the solution and aging treatment, suggesting that Orowan looping around precipitates, grain boundary strengthening, and solid solution strengthening are responsible for the high yield strength of L-DED M789. Besides, the as-fabricated alloy shows higher pitting potential than solutioned and aged sample. This work serves as a guidance for the fabrication of corrosion-resistant maraging steels by L-DED and accelerate the implementation of maraging steels for marine and offshore applications.

Keywords

Maraging steel M789; Directed energy deposition; Heat treatment; Mechanical properties; Corrosion resistance

1. Introduction

Laser-directed energy deposition (L-DED) technique is an additive manufacturing (AM) process that can create three-dimensional (3D) parts defined by computer-aided design (CAD) models. The printing head simultaneously deposits metal powders onto the substrate and melts them by using a high energy laser beam in a layer-by-layer manner [1]. Because of the high cooling rates experienced by the molten alloy during processing, parts fabricated using L-DED often have unique microstructures which consist of columnar grains that are different from those of conventionally manufactured (CM) parts [2]. The L-DED process offers a wide range of advantages, such as the capability of printing large-scale and near-net-shape parts with high deposition rates, repairing worn-out or cracked parts, and coating the surfaces [[1], [2], [3], [4]]. With the numerous advantages, many research works have been carried out on a multitude of materials that include L-DED processed Fe- [5], Ni- [6], Ti- [7], and Al-based alloys [8].

Maraging steels are a class of low carbon martensitic steels designed to have high strength and toughness property combination; these properties are derived from precipitation hardening [9]. The low carbon content makes these steels highly weldable and suitable for AM process featured by rapid cooling rates, which allows the formation of a martensitic structure during fabrication [10]. These advantages make AM maraging steels popular candidates in research. For example, Allam et al. [11] tailored the nanostructure of laser powder bed fusion (LPBF) printed maraging steel 18Ni300 through various heat treatment strategies, Deirmina et al. [12] investigated the effects of different powder atomization techniques on the fatigue properties of LPBF printed 18Ni300, and Kürnsteiner et al. [13] printed a damacus steel-like maraging steel *via* L-DED by utilizing intrinsic heat treatment (IHT).

Maraging steels are widely used in industries such as aerospace and tooling [14,15]. However, they are rarely used in marine and offshore industries because of their poor corrosion resistance as compared to other groups of steels [16]. Nevertheless, the mechanical properties of steels such as 17–4 PH, 15–5 PH, and duplex steels, which are widely used in marine and offshore applications, are not comparable to those of the maraging steels [[17], [18], [19]]. Recently, Voestalpine BÖHLER Edelstahl GmbH and Co KG developed a Co-free corrosion-resistant maraging steel M789 by replacing Co with Cr to provide the steel with improved corrosion resistance while retaining the high strength for applications in corrosive environments [20].

Despite the popularity of maraging steels, most studies are focused on LPBF processing of maraging steels. For example, Suryawanshi et al. [21] investigated the tensile, fracture, and fatigue properties of LPBF produced 18Ni300 while Paul et al. [22] examined the effect of different heat treatments on its tensile and fracture properties with particular emphasis on the fracture resistance curves. Mutua et al. [23] optimized the process parameters for LPBF printing of 18Ni300, Takata et al. [24] elucidated the crystallographic features of LPBF fabricated 18Ni300, and Bai et al. [25] studied the effects of heat treated on 18Ni300 processed *via* LPBF. However, the research on the L-DED fabrication of corrosion-resistant maraging steels is limited. Additionally, the difference in the fundamental processing characteristics of LPBF and L-DED can lead to variations in microstructure and mechanical properties of the printed parts [26,27]. Keeping this in view, a corrosion-resistant maraging steel M789 fabricated by L-DED is

examined in this study. Process parameters were optimized by varying the laser power and the scanning speed. The microstructure, mechanical properties, and corrosion resistance of both as-fabricated and heat-treated samples were analyzed.

2. Materials and methods

2.1. Powder materials

Gas-atomized spherical M789 powder with a particle size range of 45–150 μm (BÖHLER Edelstahl GmbH and Co KG) was used in this study. The chemical composition of the powder from the datasheet given by the supplier is shown in Table 1. The powder morphology was examined using a scanning electron microscope (SEM; JOEL JSM-5600LV), as shown in Fig. 1. The particles are spherical in shape with a few satellite inclusions on the surface, which were formed when small molten droplets bound on to the surface of larger particles during the gas atomization process.

Table 1. Chemical composition of maraging steel M789 powder.

Element	Fe	C	Cr	Ni	Mo	Ti	Al
wt%	Bal.	<0.02	12.20	10.00	1.00	1.00	0.60

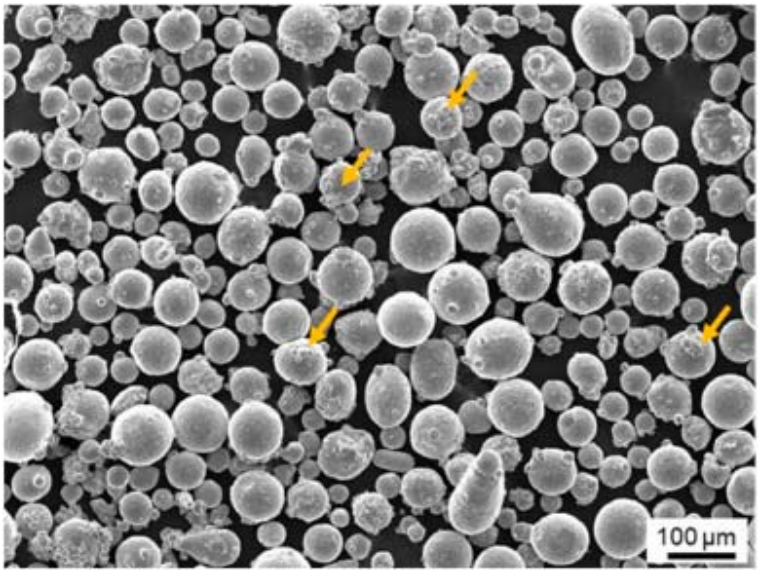

1. Download: Download high-res image (631KB)
2. Download: Download full-size image

Fig. 1. SEM micrograph of M789 powder with satellite inclusions indicated by yellow arrows. (For interpretation of the references to colour in this figure legend, the reader is referred to the Web version of this article.)

2.2. Directed energy deposition process

The identification of optimal process parameters is essential to achieve the highest possible relative densities and desired mechanical properties. Single-tracks were first printed to study the tracks' dimensions for preliminary process parameter screening, followed by printing of the blocks and the measurement of their relative densities to further determine the optimum processing window.

The samples were fabricated by a five-axis stage coaxial nozzle L-DED system (BeAM Magic 800), as schematically illustrated in Fig. 2a. The L-DED system is equipped with a Yb: Ytterbium doped fiber laser (200–2000 W) with a focal spot size of 0.75 mm. A rotating disk hopper was used to transfer the powder to the nozzle with a powder feed rate of 4 g/min. A bi-directional raster scanning strategy with 90° rotation between adjacent layers was adopted with a *z*-offset of 0.3 mm and a hatch spacing of 0.45 mm (Fig. 2b). An austenite steel block (3 × 6 × 3 mm^3) was used as the substrate. Single-tracks were printed with a power of 300–500 W and a scanning speed of 1300–1900 mm/min for preliminary process window screening, followed by printing block samples (20 × 40 × 20 mm^3). The printed blocks were separated from the substrate using an electrical discharge machine (EDM; Troop Corp, TROOP-50).

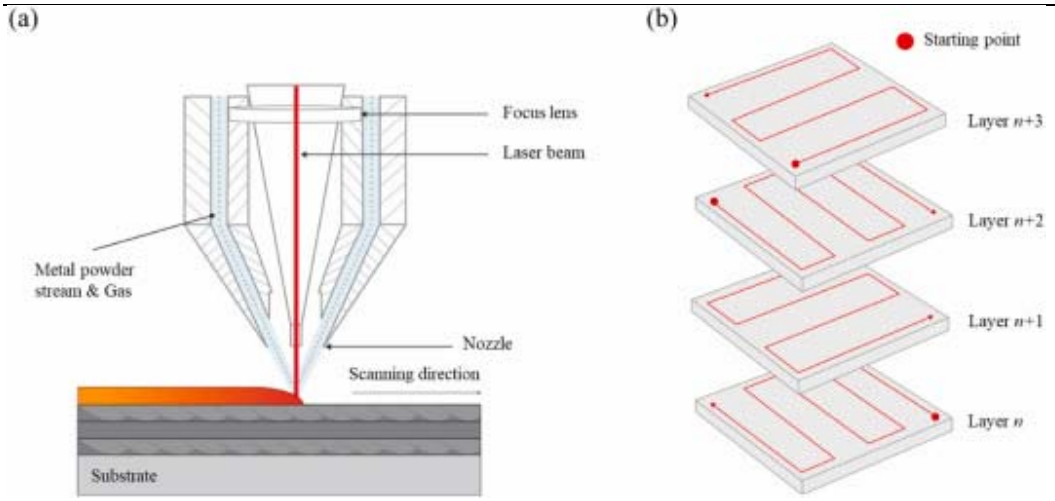

1. Download: Download high-res image (311KB)
2. Download: Download full-size image

Fig. 2. Schematic illustration of the L-DED process: (a) L-DED fabrication process and (b) the scanning strategy adopted.

2.3. Heat treatment

In this study, two heat treatment strategies, which are schematically illustrated in Fig. 3, were utilized. They were carried out in a box furnace (Elite Thermal Systems Limited, BRF 14/5–2416). In the direct aging treatment, the as-fabricated samples were directly aged at 500 °C for 2 h and subsequently air-cooled in order to trigger precipitation hardening [28]. The solution and aging treatment consists of solutionizing of the alloy at 1000 °C for 1 h with air cooling and followed by aging at 500 °C for 2 h before air cooling.

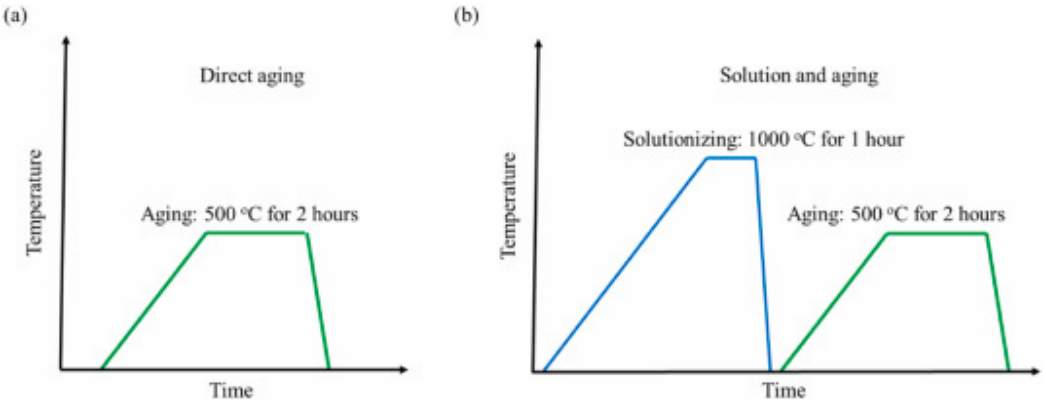

1. Download: Download high-res image (189KB)
2. Download: Download full-size image

Fig. 3. Schematic illustrations of the two heat treatment schedules employed in this work: (a) direct aging and (b) solutionizing followed by aging.

2.4. Material characterization

The L-DED printed blocks were sectioned along the build direction using EDM for subsequent microstructure analysis. X-ray diffraction (XRD; PANalytical Empyrean) with CuK_{α} radiation and a step size of 0.01° was performed over a 2θ range of 30°–90° to identify the phases present in the as-fabricated and heat-treated samples. The samples were hot mounted (Lamplan Presslam) and mechanically polished (Stuers Tegramin-25) until a mirror surface was obtained. Density measurements were conducted on the mirror surface using the image analysis method. Five random images were taken from each sample using optical microscopy (Olympus LEXT OLS4100), and an open-access image processing tool ImageJ was used to calculate the relative density [29].

The samples were then etched with the Kroll's reagent (2 mL HF, 6 mL HNO3, 92 mL distilled water) and then examined under an optical microscope (Zeiss Axioscope 2 MAT). Oxide polishing suspension (OPS) solution was used to further polish the samples for 30 min to prepare for electron backscatter diffraction (EBSD) analysis. EBSD results were collected using a field emission scanning electron microscope (FESEM; JOEL JSM-7800 F) and the grain size was calculated from the HKL Channel 5 software. The reconstruction of prior austenite grain boundaries was performed with an orientation relationship algorithm by MTEX (version 5.8.0, Institute of Mathematics) on MATLAB (Version R2021b, MathWorks, Inc.) toolbox [30].

Scanning transmission electron microscope (STEM) images were taken with a JOEL JEM-2100 F TEM equipped with an energy dispersive spectroscope (EDS). Transmission Kikuchi diffraction-EDS (TKD-EDS) analysis was performed using FESEM to analyze a larger area which could include more precipitates. Both STEM and TKD sample was prepared using a precision ion polishing system (PIPS; GATAN 691).

2.5. Mechanical testing

Tensile coupons with a thickness of 1 mm, width of 3 mm, and a gauge length of 10 mm were extracted by EDM from the printed blocks samples with the loading axis perpendicular to the build direction. Tensile tests were conducted under displacement control at a constant speed of 0.5 mm/min at room temperature by a uniaxial mechanical tester attached with a digital video extensometer (Shimadzu AGX, Japan). The as-fabricated samples were tested with a 10 kN capacity load cell while the heat-treated samples were tested with a 50 kN capacity load cell. Three identical tensile coupons were tested for each condition. Fractography of the tensile tested samples was performed using SEM. Hardness measurements were conducted with a microhardness tester (FUTURE-TECH CORP, FM-300e) with a 1 kgf load and seven indentation points were recorded from the substrate to the top of the sample.

2.6. Corrosion test

Potentiodynamic polarization tests in a 3.5 wt% NaCl solution at room temperature were conducted on the mirror polished samples with an exposed area of 1 cm^2 in an electrochemical workstation (SP300, BioLogic Ltd). A three-electrode system was used to conduct the tests with the sample set as the working electrode, a platinum sheet (20 × 20 mm^2) as the counter electrode, and an Ag/AgCl electrode (electrode potential of 0.197 V in saturated KCl solution versus standard hydrogen electrode) as the reference electrode. Potentiodynamic polarization curves were obtained at a rate of 20 mV/min from −500 to 500 mV, and the results were subsequently analyzed using the EC-lab software.

3. Results and discussion

3.1. Process parameter optimization

3.1.1. Single track printing

Single-track printing and characterization allow for a rapid screening of the process parameter combinations for the identification of suitable one and eliminate the unsuitable ones before block printing. Fig. 4a shows the single-track process parameter map obtained from this study with the representative examples of satisfactory and unsatisfactory single-track geometries. It is essential to obtain melt pool dimensions that can satisfy the dilution criterion by determining the penetration *P* and height *H* (Fig. 4a) [31]. Herein, the effects of power and speed can be observed: a low power and high scanning speeds (*i.e.*, 300 W and 1700–1900 mm/min) result in insufficient penetration of the bead into the substrate, while a medium power and medium to high scanning speeds (*i.e.*, 400 W and 1500–1900 mm/min) produce sufficient penetration into the substrate. A further increase in the laser power (*i.e.*, to 500 W) leads to spattering because of the instability in the melt pool, which recoils molten liquid onto the surrounding and results in nozzle clogging [32].

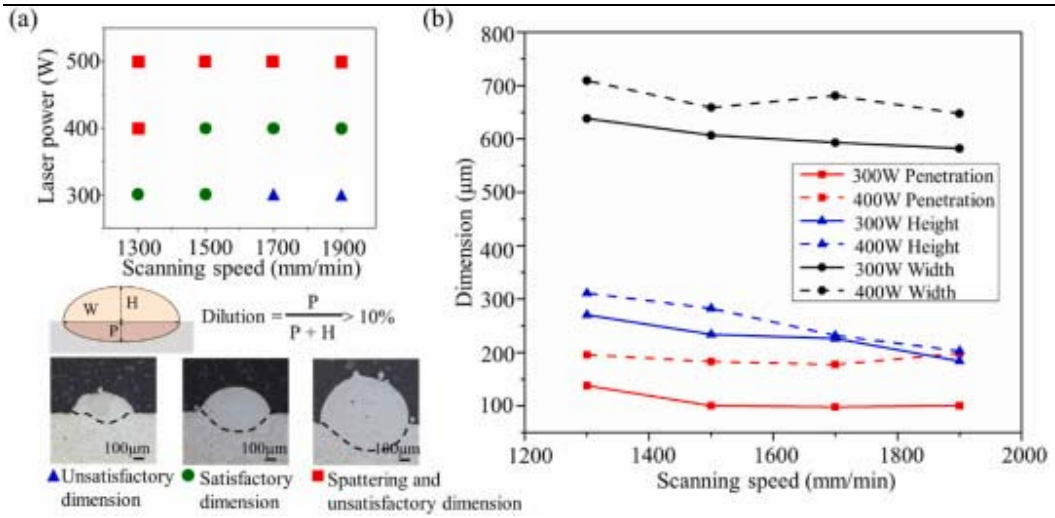

1. Download: Download high-res image (370KB)
2. Download: Download full-size image

Fig. 4. Single-track printing of M789 *via* L-DED: (a) process parameter map with representative morphologies of L-DED printed single-tracks and (b) effects of laser power and scanning speed on the dimension of single-tracks.

Fig. 4b shows the influence of laser power and scanning speed on the single-track dimensions. An increase in laser power produces a larger single-track dimension because of the increase in energy density introduced into the melt pool. An increase in scanning speed reduces the single-track's width and height because of less powder deposition and reduced laser–powder interaction time. In contrast, the penetration does not significantly vary with increasing scanning speed.

3.1.2. Block printing

Fig. 5 shows the process parameter matrix for block printing based on single-track process parameters. Spattering is observed at high power (*i.e.*, 500 W) because of the excessive energy input, which increased the chances of void formation and nozzle damage [14]. Six samples labeled from 1 to 6 were used for relative density measurements (Fig. 5). As shown in Fig. 6a, all the samples exhibit a relative density of >99%. A higher laser power with a constant scanning speed leads to a higher relative density because of the deeper penetration of the molten metal and more remelting of previous layers, ensuring good bonding and elimination of trapped gasses. In contrast, an increase in scanning speed results in a lower relative density because of the insufficient laser–powder interaction time to fully melt the deposited powder for proper metallurgical bonding. Two types of pores are observed in the samples: spherical gas pores and irregularly shaped lack-of-fusion pores (Fig. 6b and c). Gas pores can arise from the gas trapped in the powder or shielding gas during the fabrication process. Lack-of-fusion pores are formed because of the insufficient bonding between tracks or layers as a result of incorrect *z*-direction increment, hatch spacing, or insufficient energy input [1]. Sample 5 was selected for further microstructural and mechanical characterization because it exhibits the highest relative density of 99.86 ± 0.04% amongst all the process parameter combinations explored.

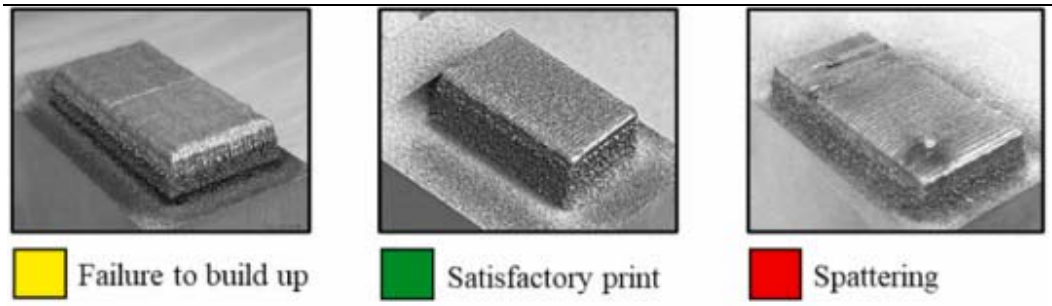

Speed (mm/min) \ Power (W)	300	400	500
1500	1	4	
1700	2	5	
1900	3	6	

1. Download: Download high-res image (455KB)
2. Download: Download full-size image

Fig. 5. Process parameter matrix for the L-DED fabrication of M789 samples with representative images showing the block samples printed under different processing parameters.

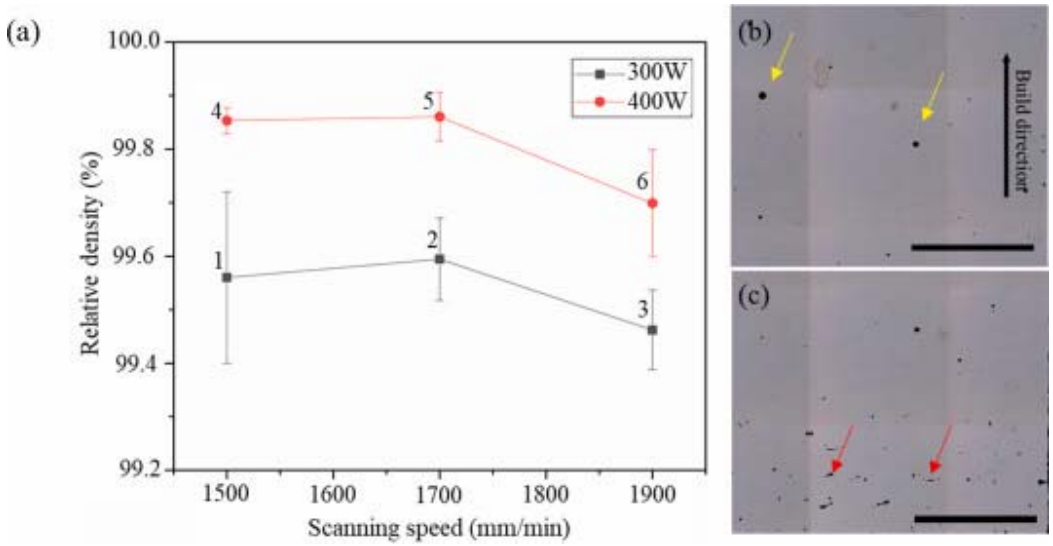

1. Download: Download high-res image (315KB)
2. Download: Download full-size image

Fig. 6. (a) Relative density measurements of samples 1–6. Type of pores found in L-DED printed parts: (b) gas pores indicated by yellow arrows and (c) lack-of-fusion pores indicated by red arrows. Scale bars: 2 mm. (For interpretation of the references to colour in this figure legend, the reader is referred to the Web version of this article.)

3.2. Microstructural analysis

The optical micrographs displayed in Fig. 7 provide an overview of the microstructures of the as-fabricated, directly aged, solutioned, and solutioned and aged samples. The as-fabricated sample exhibits fish scale-like melt pool boundaries that alternate with layers (Fig. 7a), which are produced by the raster scanning pattern with 90° rotations between each adjacent layer (Fig. 2b). The fish scale-like melt pool boundaries can still be observed after direct aging treatment (Fig. 7b) but become invisible after solution and solution and aging treatments (Fig. 7c and d).

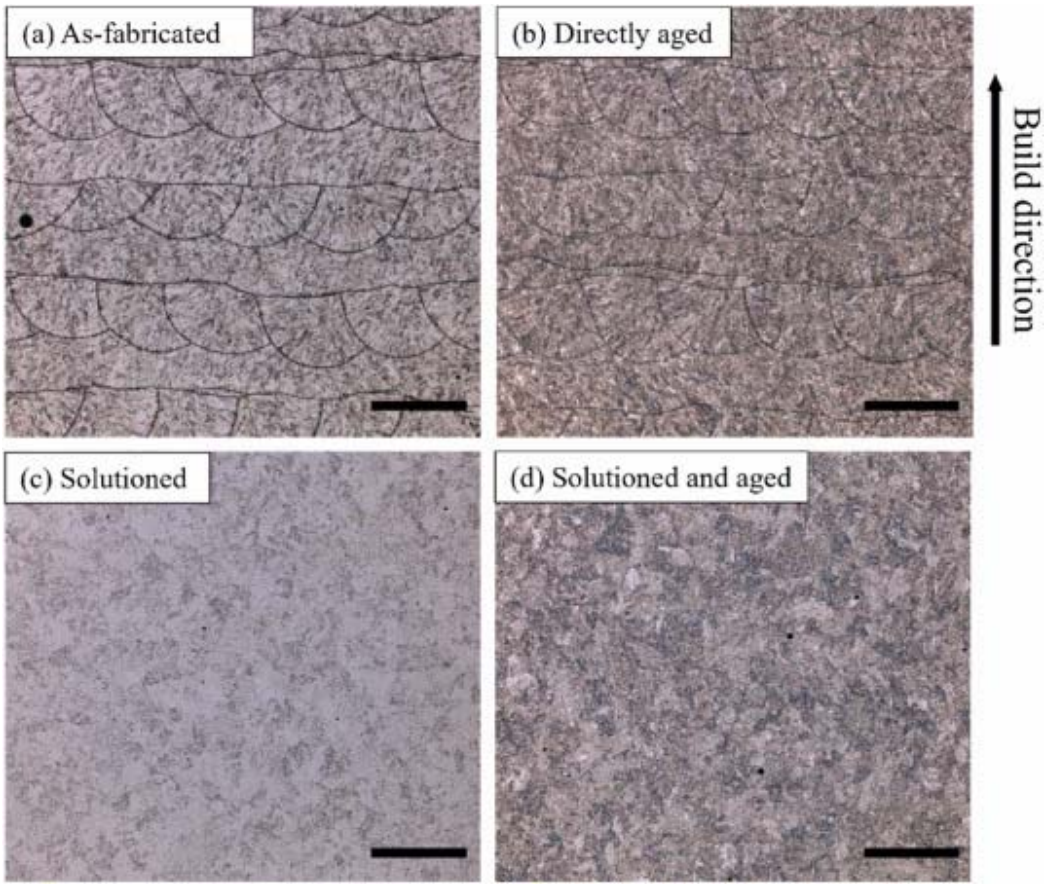

1. Download: Download high-res image (2MB)
2. Download: Download full-size image

Fig. 7. Optical micrographs of M789 block samples: (a) as-fabricated, (b) directly aged, (c) solutioned, and (d) solutioned and aged conditions. Scale bars: 500 μm.

The XRD scans obtained on the as-fabricated, directly aged, and solutioned and aged samples are shown in Fig. 8. The (110), (200), and (211) diffraction peaks reveal a dominant martensitic phase in all the samples. However, a (111) peak appears in the XRD scan of the directly aged sample, implying the formation of austenite phase during the direct aging treatment. In contrast, no (111) peaks were observed in the solutioned and aged sample, indicating that no reversion of martensite to austenite has taken place during the aging process after solutionizing.

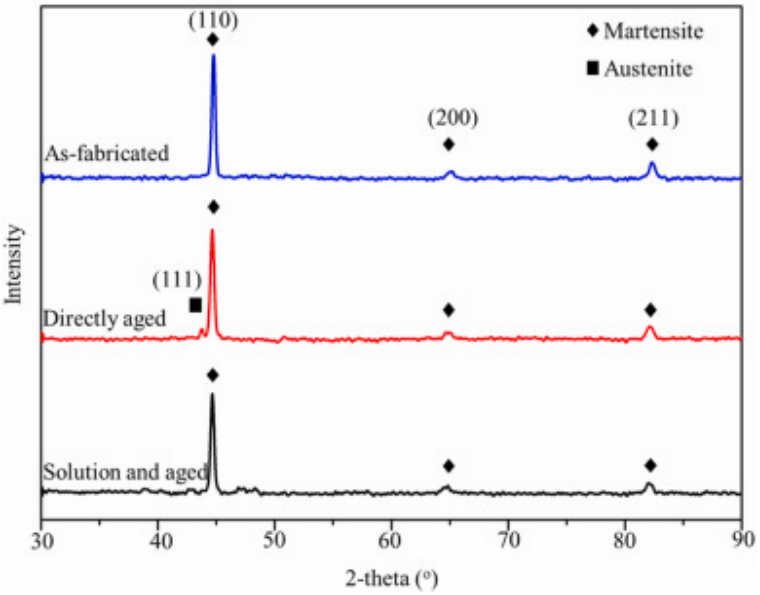

1. Download: Download high-res image (243KB)
2. Download: Download full-size image

Fig. 8. XRD profiles of L-DED as-fabricated, directly aged, and solutioned and aged samples of maraging steel M789.

Fig. 9 shows the EBSD results for the as-fabricated, directly aged, and solutioned and aged samples. Inverse pole figure (IPF) maps obtained in the IPF-X orientation for the cross section along the build direction reveal the grain orientations and morphologies in them. A martensitic structure is observed across all the three samples (Fig. 9a–c). The IPF of the as-fabricated sample depicts a strong <111> texture orientated towards the center of the melt pool, but the grains do not cross the individual melt pool boundaries (Fig. 9a). In addition, a maximum uniform density (MUD) of 1.54 suggests a random grain texture. In contrast, the martensitic grains from the solutioned and aged sample exhibit a random texture with no distinguishable melt pool boundaries (Fig. 9c). The reconstructed prior austenite grains (PAG) maps from the as-fabricated and directly aged samples reveal two different PAG structures within the melt pool: elongated grains near the melt pool boundaries and equiaxed grains at the center of the melt pool (Fig. 9d and e). The PAG map obtained on the as-fabricated sample exhibits a strong <110> texture which can be estimated from the Kurdjumov–Sachs (K–S) orientation relationship between the martensite and PAGs and can be expressed as $<110>_{austenite}//<111>_{martensite}$ (Fig. 9a) [33]. In contrast, the solutioned and aged sample reveals large equiaxed PAGs, which are similar to conventional maraging steels (Fig. 9f) [26].

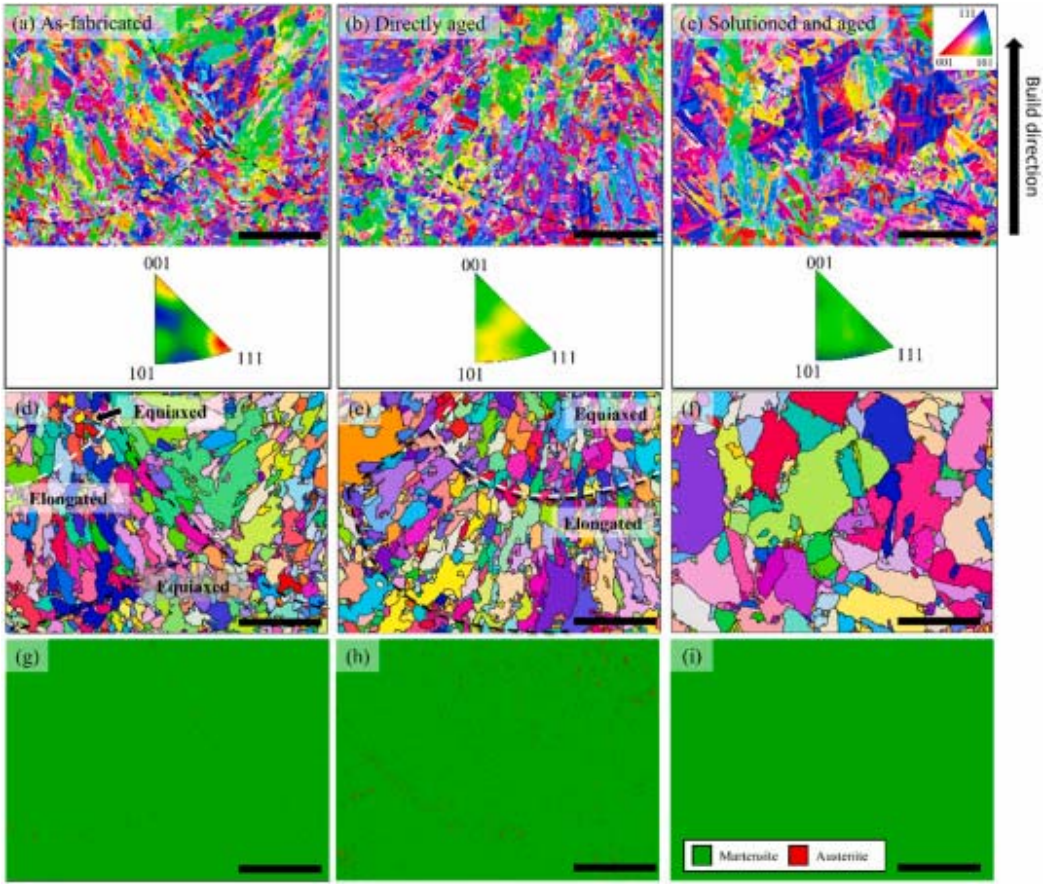

1. Download: Download high-res image (2MB)
2. Download: Download full-size image

Fig. 9. EBSD analysis of maraging steel M789: IPF maps and IPFs of (a) as-fabricated, (b) directly aged, and (c) solutioned and aged samples, with their corresponding reconstructed PAG maps from (d) to (f) and phase maps from (g) to (i). Scale bars: 100 μm.

EBSD phase maps reveal minimal austenite phases (volume fraction of 0.16%) along the melt pool boundaries in the as-fabricated sample (Fig. 9g), while an increased amount of austenite phase (volume fraction of 1.36%) is observed in the directly aged sample (Fig. 9h). In contrast, no austenite phase is present in the solutioned and aged sample (Fig. 9i). The IPF and phase maps are in good agreement with the XRD results shown in Fig. 8. However, no (111) austenite peaks are present in the as-fabricated XRD measurements because of the detection limit of conventional XRD [34].

3.3. TEM analysis

Further microstructural analysis of the solutioned and aged sample was performed using a STEM. Results are shown in Fig. 10. Bright field-TEM (BF-TEM) image reveals a lath-like structure within the matrix (Fig. 10a). Additional dark field-TEM (DF-TEM) image (Fig. 10b) confirms it to be martensite with an interplanar spacing of 2.027 Å, as reflected by the corresponding selected area electron diffraction (SAED) pattern. Only the martensites aligned to the zone axes are visible in the TEM images. High resolution-TEM

(HR-TEM) image (Fig. 10c) of the martensite lath shows the lattice boundary and an interplanar spacing of 2 Å. The martensitic structure revealed by TEM is in good agreement with the XRD measurements and EBSD phase maps (Figs. 8 and 9i). STEM-EDS maps reveal spherical Ti- and Al-rich precipitates embedded in the matrix and are surrounded by dislocations in Fig. 10d and e. Dislocations are commonly found in low carbon martensitic steels which can be distinguished by the dark areas and entanglements around the precipitates and matrix [35]. Additional TKD-EDS analysis of the solutioned and aged sample is shown in Fig. 11. The spherical precipitates (190–220 nm in diameter) are distributed within the martensites (Fig. 11a). TKD-EDS maps show that the precipitates are mainly Ti-rich (Fig. 11b). A higher magnification TKD-EDS map (Fig. 11c) reveals the presence of Al within the Ti-rich precipitate, which is in agreement with the STEM-EDS maps in Fig. 10e.

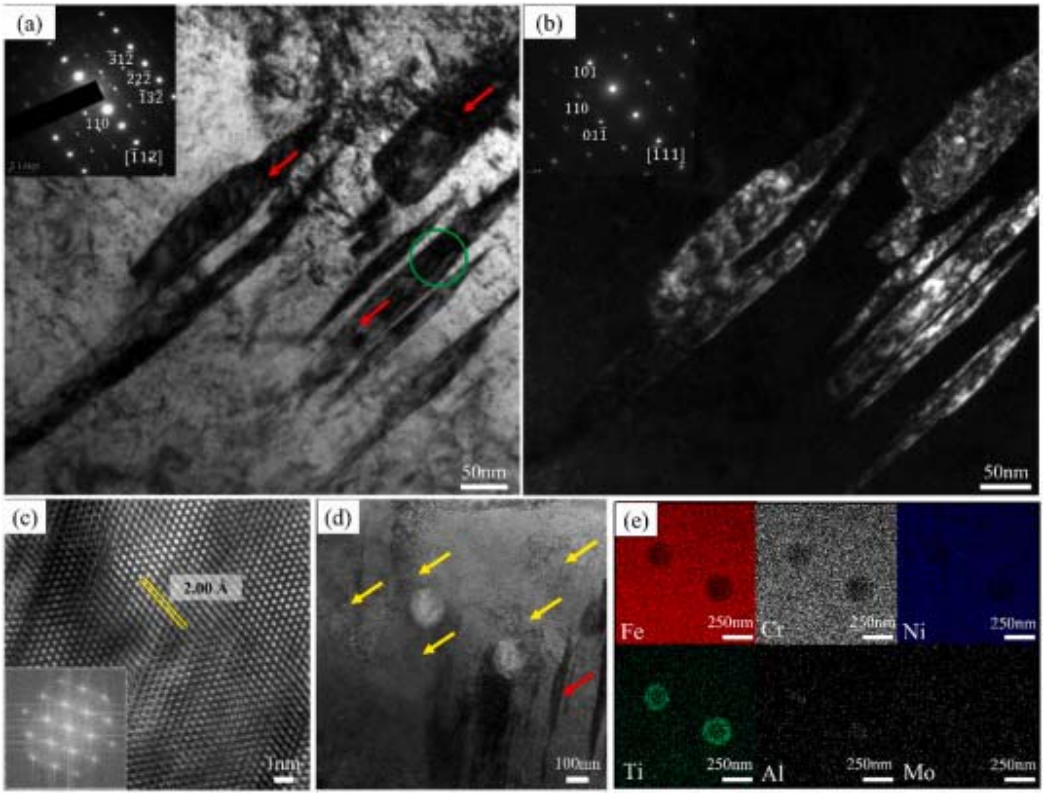

1. Download: Download high-res image (1MB)
2. Download: Download full-size image

Fig. 10. TEM and STEM images of solutioned and aged sample: (a) BF-TEM image of martensite laths (red arrows), (b) DF-TEM image of martensite laths with the corresponding SAED pattern of the region circled in green, (c) HR-TEM image of the martensite lath with its corresponding fast Fourier transform, (d) BF-STEM image, and (e) STEM-EDS maps of the spherical precipitates. The dislocations are indicated by yellow arrows. (For interpretation of the references to colour in this figure legend, the reader is referred to the Web version of this article.)

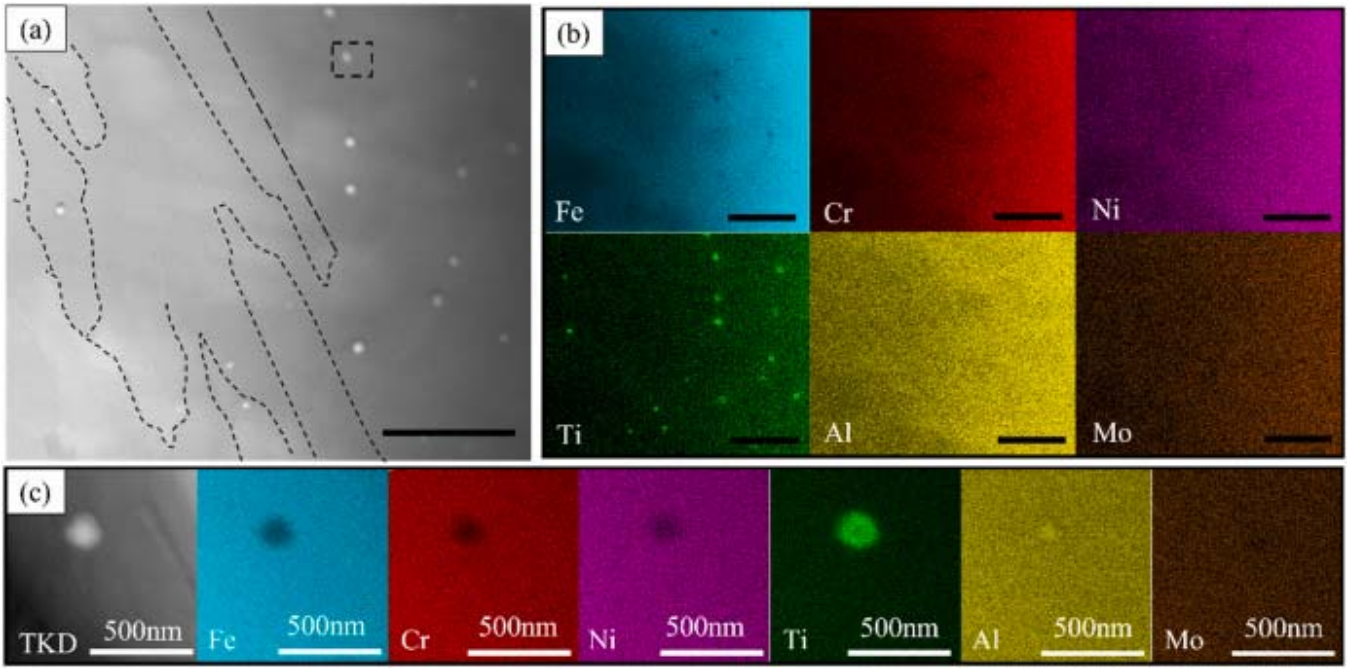

1. Download: Download high-res image (2MB)
2. Download: Download full-size image

Fig. 11. TKD-EDS mapping of solutioned and aged sample: (a) image overview, (b) EDS map that reveals a cluster of Ti-rich precipitates, and (c) high magnification of TKD-EDS map that reveals the particle is rich in Ti and Al. Black scale bars: 2.5 μm.

The Ti-rich precipitates that form rapidly could serve as nucleation sites for the Al precipitates during heat treatment, leading to the formation of the observed Ti- and Al-based precipitates [9]. However, the sluggish Mo precipitation kinetic prevents the formation of Mo-based precipitates within a short aging time, resulting in the absence of Mo in these precipitates (Fig. 10, Fig. 11b) [36]. Precipitates in LPBF printed M789 after solution and aging treatment mainly consisted of two different morphologies by using an atom probe tomography: plate and spherical precipitates [37].

3.4. Mechanical properties

A summary of the mechanical properties of the as-fabricated, directly aged, and solutioned and aged sample 5 is provided in Table 2. The as-fabricated sample shows a hardness value of 312 ± 6 HV. An increase of 69% and 73% in hardness of this sample was achieved by direct aging, and solution and aging treatment, respectively. The hardness values were uniform along the build direction (Fig. 12).

Table 2. Summary of mechanical properties for maraging steel M789.

Sample	Vickers hardness (HV)	Yield strength (MPa)	Ultimate tensile strength (MPa)	Elongation to failure (%)	Young's modulus (GPa)
As-fabricated M789	312 ± 6	650 ± 20	1057 ± 7	15 ± 1	113 ± 7
Directly aged M789	519 ± 10	1350 ± 56	1512 ± 54	13 ± 3	149 ± 15
Solutioned and aged M789	540 ± 6	1500 ± 80	1683 ± 24	8 ± 1	200 ± 25
LPBF as-fabricated M789[a]	306–313	795 ± 32	1070 ± 34	17 ± 3	–
LPBF solution and aged M789[a]	538–552	1714 ± 13	1798 ± 4	9 ± 2	–
L-DED as-fabricated18Ni300[b]	350	–	959 ± 20	15	–
L-DED solution and aged18Ni300[b]	533	–	1561 ± 16	11.5	–

a Data from Tian et al. [28].

b Data from Yao et al. [41].

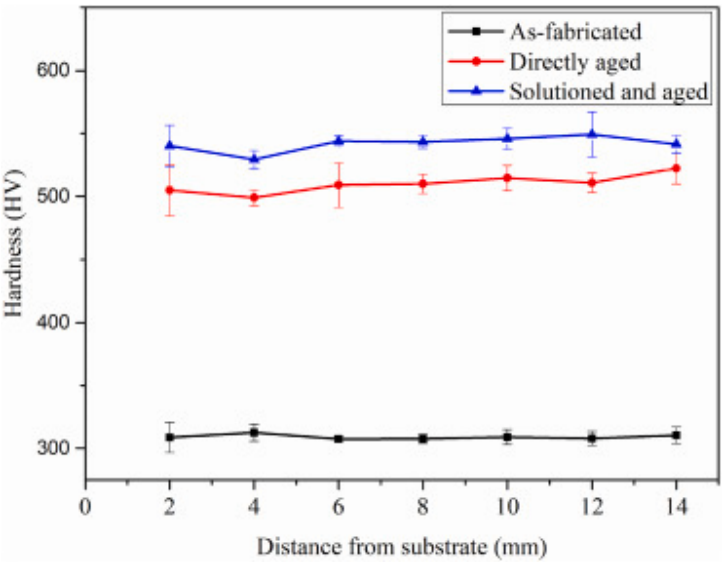

1. Download: Download high-res image (272KB)
2. Download: Download full-size image

Fig. 12. Hardness profiles of as-fabricated, directly aged, and solutioned and aged samples.

Fig. 13a shows the representative tensile stress-strain responses of the as-fabricated, directly aged, and solutioned and aged samples. On average, direct aging treatment improves the ultimate tensile strength (UTS) and yield strength (YS) by 43% and 107%, respectively, but reduces the elongation to failure by 13%. In contrast, the solution and aging route results in an increase of 59% and 130% in UTS and YS, respectively, but at the cost of a 44% decrease in elongation to failure. A comparison of L-DED fabricated M789 with L-DED fabricated 18Ni300 and LPBF fabricated M789 is also shown in Table 2. The tensile strengths of the maraging steels after solution and aging treatment ranked in ascending order are the following: L-DED 18Ni300, L-DED M789, LPBF M789. Fig. 13b shows the work hardening rate curves of the as-fabricated and heat-treated sample 5. Sample 5 is chosen for further analysis as it exhibits the highest UTS in all three conditions. The work hardening rate curves are characterized by two stages. In stage 1 (S1), the work hardening rate drastically decreases in all the samples, which is attributed to the dynamic recovery of dislocations [38]. In stage 2 (S2), the work hardening rate gradually decreases in the as-fabricated, and solutioned and aged samples. The directly aged sample exhibits a nearly constant work hardening rate. Lastly, the work hardening rate sharply decreases until failure for all samples. The higher work hardening rate in the as-fabricated sample than that of the solutioned and aged sample corresponds to the higher elongation to failure [39]. Additionally, the slow decrease in the work hardening rate in S2 for the directly aged sample could be associated with the transformation-induced plasticity effect from the reverted austenite [40]. The negative work hardening rate is the result of achieving maximum tensile stress in which the work hardening rate equals zero and thus, signifying the onset of necking.

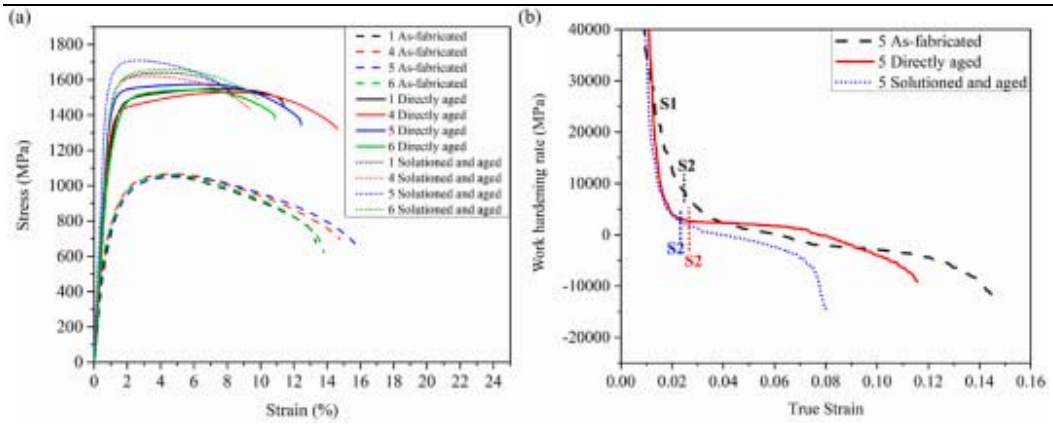

1. Download: Download high-res image (352KB)
2. Download: Download full-size image

Fig. 13. Mechanical properties of maraging steel M789 samples: (a) tensile curves and (b) work hardening rate curves of the as-fabricated, directly aged, and solutioned and aged sample 5.

3.5. Fractography

The fractographs obtained from the fractured tensile coupons of as-fabricated, directly aged, and solutioned and aged samples are shown in Fig. 14. The differences in fracture morphology between the three samples correspond to the increase in UTS and decrease

in elongation to fracture (Table 2). The as-fabricated sample exhibits a high degree of plastic deformation, as seen from the low magnification image (Fig. 14d). Fine dimples can be observed at higher magnification (Fig. 14g), depicting a ductile fracture behavior. After direct aging treatment, fine dimples continue to dominate the fracture surface, as also reflected by the minimal decrease in elongation of about 2%. However, river patterns can be observed, which indicates cleavages (Fig. 14h). Pores can be observed on the fracture surfaces of the as-fabricated and directly aged samples (Fig. 14d and e). The high UTS and low elongation to failure in solutioned and aged samples suggest a mixture of ductile and brittle failure which is depicted by the increased presence of cleavages, while some fine dimples indicate localized plastic deformation in certain regions (Fig. 14i).

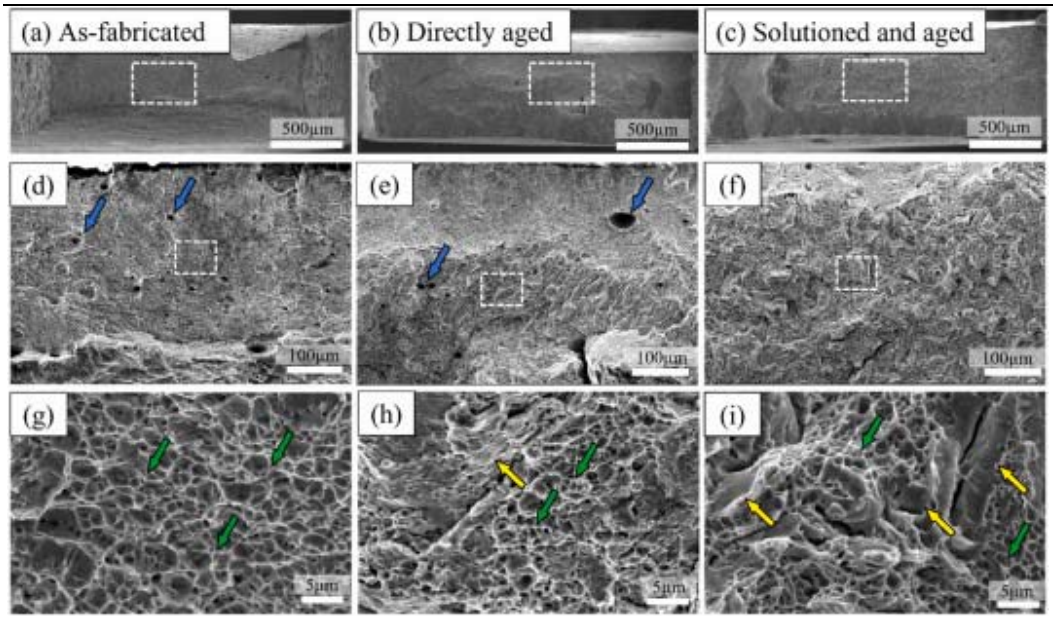

1. Download: Download high-res image (1MB)
2. Download: Download full-size image

Fig. 14. Fractography of sample 5: overview images of the sample in (a) as-fabricated, (b) directly aged, and (c) solutioned and aged conditions with (d) to (f) their low magnification images and (g) to (i) their high magnification images. The pores, dimples, and cleavages are indicated by blue, green, and yellow arrows, respectively. (For interpretation of the references to colour in this figure legend, the reader is referred to the Web version of this article.)

3.6. Corrosion resistance

The potentiodynamic polarization measurements made on the M789 samples are shown in Fig. 15. Metastable pitting can be observed along the upper region of the curves, which indicates that new passive films are generated over the metastable pits, as investigated by Ref. [42]. As the applied potential increases above 0.34 V for the as-fabricated sample and 0.31 V for the directly aged, and solutioned and aged samples, the corrosion current density i_{corr} increases substantially, which implies a breakdown of the passive film and the formation of stable pits, known as the pitting potential E_p [43]. The corrosion

potential E_{corr} and i_{corr} for the as-fabricated sample are −0.18 V and 15.48 × 10^{-7} A/cm^2 respectively, the solutioned and aged sample has an E_{corr} of −0.21 V and an i_{corr} of 4.36 × 10^{-7} A/cm^2, and the directly aged sample has an E_{corr} of −0.21 V and an i_{corr} of 4.89 × 10^{-7} A/cm^2. The lower i_{corr} value suggests that the solutioned and aged, and directly aged samples have a lower corrosion rate (and hence a higher corrosion resistance) as compared to the as-fabricated sample. The higher corrosion rate of the as-fabricated sample could be the result of microsegregation during printing which has a negative impact on the corrosion properties. Nevertheless, both samples have lower corrosion rates as compared to LPBF fabricated maraging steel 18Ni300 [44].

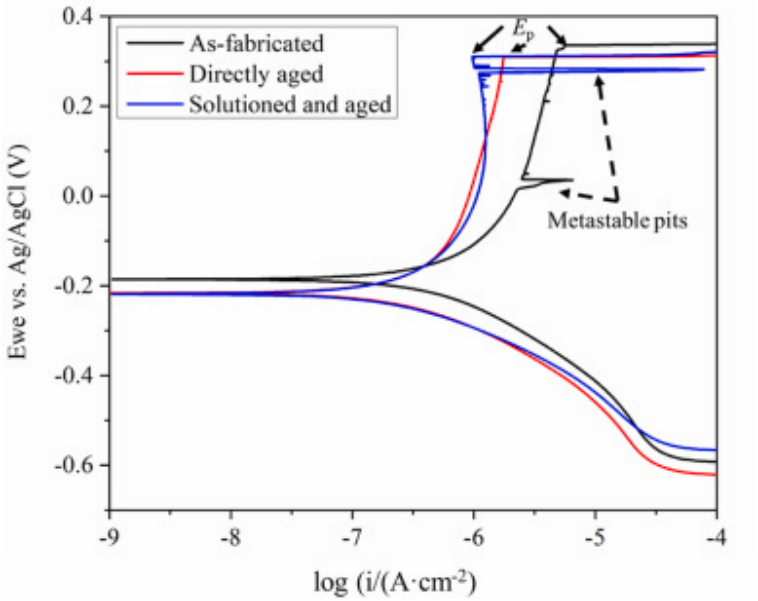

1. Download: Download high-res image (270KB)
2. Download: Download full-size image

Fig. 15. Potentiodynamic polarization curves of as-fabricated, directly aged, and solutioned and aged M789. (For interpretation of the references to colour in this figure legend, the reader is referred to the Web version of this article.)

The higher E_p in the as-fabricated sample can be attributed to the presence of the austenite phase around the melt pool boundaries (Fig. 9g) [45]. In addition, the presence of precipitates (shown in Fig. 11b) could reduce E_p, because pitting corrosion tends to initiate from defects or non-uniformities in the passive film such as pores and precipitates within the matrix which may result in a lower E_p for the directly aged, and solutioned and aged samples [45,46]. Nevertheless, M789 steel printed by L-DED exhibit a higher E_p as compared to L-DED as-fabricated 15–5 PH steel [41], and LPBF printed 15–5 PH steel followed by heat treatment [45].

4. Discussion

4.1. Grain structure formation

The microstructure of the as-fabricated sample results from the solidification behavior and phase transformation from austenite to martensite during L-DED printing. The reconstructed PAG maps give a glimpse of the initial grain growth and solidification process during printing (Fig. 9d). During the initial deposition and solidification stage, elongated austenite grains grow along the highest thermal gradient towards the center of the melt pool boundary (Fig. 16) [47]. Subsequent cooling triggers the martensite transformation inside each PAG when the sample temperature is below the martensite start temperature. The martensite grains grow in a variety of possible crystallographic orientations that can be determined by the K–S orientation relationship, thus forming random grain texture in the as-fabricated sample [24,48,49].

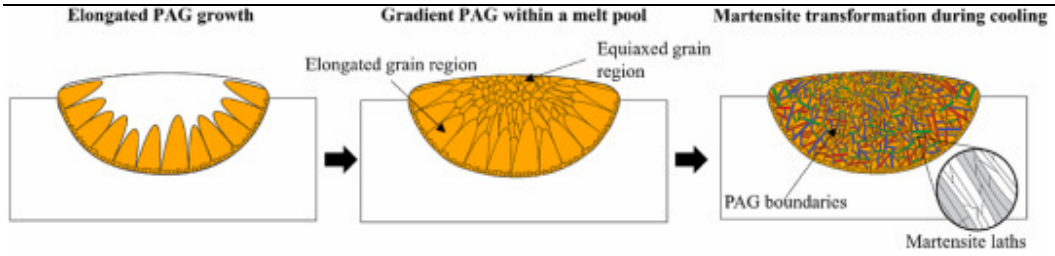

1. Download: Download high-res image (323KB)
2. Download: Download full-size image

Fig. 16. Schematic illustration of microstructural evolution of M789 during L-DED fabrication.

The non-uniform temperature distribution during the L-DED processing can cause microsegregation of the alloying elements and enrichment of austenite stabilizer elements, such as Ni along the melt pool boundaries [26]. Nevertheless, the low Ni content in maraging steel M789 could be the reason for the reduced volume fraction of austenite in the as-fabricated sample as compared to L-DED printed 18Ni300 [26]. The microsegregation of the austenite stabilizer elements further promotes the reversion of martensite to austenite in localized areas of the melt pool after the direct aging treatment because the aging temperature of 500 °C was insufficient to homogenize and diffuse the elements to eliminate the microsegregation [11,23]. However, solution treatment at 1000 °C can homogenize the alloying elements because of the increased diffusivity at higher temperatures [12]. This leads to the elimination of the melt pool boundaries, formation of equiaxed PAG, and suppression of reversion to austenite during subsequent aging treatment (Fig. 9c, f, and i). However, prolong aging of maraging steels (*e.g.*, >9 h at 500 °C for M789) even after solutionizing can lead to martensite reversion into austenite and precipitation coarsening [50], which is known as overaging, resulting in the softening of them.

4.2. Strengthening mechanism

Precipitation hardening is the main strengthening mechanism for maraging steel M789, as commonly reported in the studies of AM fabricated maraging steels [14,21,51]. At the same time, the martensite grain size can also influence the mechanical properties of maraging steels through grain boundary strengthening [52,53]. The presence of precipitates within the martensite matrix (Fig. 11a) suggests that both the grain boundary strengthening (quantified *via* the Hall–Petch relationship) and Orowan strengthening are contributors as the grain size is larger than the average precipitate spacing [54]. In addition, alloying elements that exist as solid solutions within the matrix distort the atomic lattice because of the misfit of atomic radius, which prevents the movement of dislocation and leads to solid solution strengthening [55]. The synergetic effects of grain boundary strengthening, precipitation strengthening, and solid solution strengthening in the maraging steel M789 can be expressed as

$$\sigma_{\mathrm{y}} = \sigma_{\mathrm{Mart}} + \sigma_{\mathrm{p}} + \sigma_{\mathrm{ss}} \tag{1}$$

in which σ_{y} is the yield strength of the alloy, σ_{Mart} is the strength of the martensite matrix, σ_{p} is the strength from the precipitates, and σ_{ss} is the strength from solid solutions.

The strength of the martensite is influenced by the Hall–Petch relationship and the Taylor equation accounting for the dislocation density within the martensite matrix [56]. Thus, the strength of the martensite matrix can be expressed as

$$\sigma_{\mathrm{Mart}} = 300 d^{-\frac{1}{2}} + 0.25 M \mu b \rho^{\frac{1}{2}} \tag{2}$$

in which d (~4 μm) is the effective grain size from the martensite, as derived from Fig. 9c, μ is the shear modulus (~77 GPa for a Fe–Ni matrix) [57], M the Taylor orientation factor (= 3), b is the burgers vector (= 0.249 nm) [56], and ρ is the dislocation density (~9.4×10^{14} m^{-2}) [58]. Therefore, the estimated contribution from the martensites is calculated to be 579 MPa.

The sizes of the precipitates in Figs. 10 and 11 are greater than the critical radius R_{crit} ($R_{\mathrm{crit}} = 15b$, where b = 0.249 nm) [46]. Therefore, the strengthening contribution of the precipitates σ_{p} can be expressed by using the Orowan equation [59]:

$$\begin{cases} \sigma_{\mathrm{p}} = \dfrac{\mu b}{2\pi K(\lambda - d)} \ln\left(\dfrac{\lambda - d}{2b}\right) \\ \dfrac{1}{K} = \dfrac{1}{2}\left(\dfrac{1}{1-\upsilon} + 1\right) \end{cases} \tag{3}$$

in which μ is the shear modulus (~71 GPa), λ is the calculated interspacing of the precipitates (~212 nm), K is a function of the Poisson's ratio υ (= 0.3) [59], and d is the average precipitate size (~200 nm). Therefore, the estimated contribution of the precipitates is calculated to be 598 MPa.

Solid solution strengthening can prevent the movement of dislocations from the misfits of atomic radius from the alloying elements such as Ni, Ti, and Mo. Thus, the strengthening of solid solutions can be expressed as [56]:

$$\sigma_{SS} = \sum_i \left(\beta_i^2 x_i\right)^{\frac{1}{2}} \quad (4)$$

in which β_i is the strengthening constant related to the lattice and modulus misfit of the respective elements and xi is the atomic fraction of the respective substitutional elements. Table 3 shows the values of β_i from the work of Li et al. [60] and xi. Therefore, the contribution *of* solid solution strengthening is estimated to be 311 MPa. Hence, the total contribution of YS from σ_{Mart}, σ_p, and σ_{ss} is calculated to be 1488 MPa, which is close to the measured YS of ~1500 MPa.

Table 3. Values of β_i and xi of the respective elements for solid solution strengthening in maraging steel M789 [60].

Elements	Ni	Ti	Mo
β_i	322	1010	1057
xi	9.55	1.17	1.24

4.3. Mechanical properties

The similar hardness along the build direction of the as-fabricated sample shown in Fig. 12 suggests that no IHT or precipitation hardening occurred in the lower layers during fabrication, which is different from L-DED fabricated 18Ni300 [23]. The absence of Co in maraging steel M789 could be the reason for the absence of IHT, as Co could enhance the precipitation kinetics in maraging steels [48]. A hardness of ~312 HV in the as-fabricated sample is expected because of the absence of C, leading to a soft Fe–Ni martensite matrix of ~300 HV [9].

The increase in UTS, YS, and decrease in ductility after direct aging and solution and aging treatments are caused by the strength–ductility trade-off from the precipitation hardening in the Fe–Ni martensite matrix during heat treatment (Table 2) [11,12,23]. As compared to the directly aged sample, the higher UTS of solutioned and aged sample can be attributed to the homogenous elemental distribution after solutionizing, which leads to a higher amount of supersaturated elements to trigger the formation of more precipitates. In contrast to the solutioned and aged sample, the microsegregation of elements such as Ni in the directly aged sample promoted the reversion of martensite to austenite, which reduces the UTS and depletes the supersaturated elements required for the precipitation [11].

Interestingly, the directly aged sample has a significant increase in UTS (by ~450 MPa) with only a slight reduction in the elongation to failure (by ~2%) as compared to the as-fabricated sample, while solutioned and aged sample achieved a higher UTS (by ~630 MPa) by sacrificing its elongation substantially (by ~7%). As austenite can increase the ductility while reducing the tensile strength of a material [37], the introduction of a small volume fraction of austenite phase into the martensite matrix allows the steel to achieve good ductility while maintaining high strength from the precipitates. However, additional research is required for the optimization of austenite volume fraction.

The difference in mechanical properties of L-DED and LPBF printed M789 samples shown in Table 2 could be primarily attributed to the difference in grain size [50]. From

equation (2), larger martensite grains lead to a lower YS according to the Hall–Petch relationship. L-DED fabricated samples generally have larger grain sizes than their LPBF printed counterparts because of the larger laser spot size and slower cooling rates (10^2–10^4 K/s for L-DED *vs* 10^5–10^7 K/s for LPBF), resulting in a lower tensile strength [[61], [62], [63]]. In this study, the martensite grains have an average grain size of ~4 μm as compared to other LPBF fabricated maraging steel of 1–2 μm [23,44], which could be the underlying reason for the lower YS and UTS.

5. Conclusions

In this study, L-DED was used to fabricate corrosion-resistant maraging steel M789. The samples were subjected to two heat treatment conditions: direct aging, and solution and aging treatments. The microstructure, and mechanical and corrosion properties of the as-fabricated, directly aged, and solutioned aged samples were evaluated.

A laser power of 400 W and scanning speed of 1700 mm/min were chosen as the optimal process parameters to print nearly fully dense parts, which could achieve a UTS of ~1057 MPa and elongation to failure of ~15%. The blocks fabricated at a low power failed to build up, while a high power led to spattering and nozzle damage.

Direct aging treatment could not homogenize the elements and eliminate microsegregation, thus increasing the volume fraction of austenite phases. However, solutionizing at 1000 °C could homogenize the elements and suppress the reversion of martensite to austenite during aging treatment.

The solutioned and aged sample achieved the highest UTS of ~1683 MPa due to the grain boundary strengthening, precipitation strengthening, and solid solution strengthening. However, its elongation to failure was reduced to ~8% due to the strength–ductility trade-off. Compared to its LPBF solutioned and aged counterparts, the L-DED solutioned and aged M789 has a lower tensile strength due to the larger martensite grains formed.

Potentiodynamic polarization tests revealed higher pitting potential of the samples in both as-fabricated and solutioned and aged conditions as compared to L-DED and LPBF processed 15–5 PH steel. The presence of austenite and absence of precipitates in the as-fabricated sample contributes to a higher pitting potential than that of the solutioned and aged sample.

CRediT authorship contribution statement

Yung Zhen Lek: Conceptualization, Data curation, Methodology, Writing – original draft. **Chengcheng Wang:** Conceptualization, Methodology, Validation, Writing – review & editing. **Xiaojun Shen:** Methodology. **Ze Chen:** Methodology. **Upadrasta Ramamurty:** Writing – review & editing. **Kun Zhou:** Conceptualization, Funding acquisition, Methodology, Project administration, Supervision, Validation, Writing – review & editing.

Declaration of competing interest

The authors declare that they have no known competing financial interests or personal relationships that could have appeared to influence the work reported in this paper.

Acknowledgement

This research is supported by the National Research Foundation, Prime Minister's Office, Singapore under its Medium-Sized Center funding scheme and Agency for Science,

Technology and Research, Singapore via the Structural Metal Alloys Programme (No. A18B1b0061).

Data availability

Data will be made available on request.

References

[1]

D. Svetlizky, M. Das, B. Zheng, A.L. Vyatskikh, S. Bose, A. Bandyopadhya y, J.M. Schoenung, E.J. Lavernia, N. Eliaz

Directed energy deposition (DED) additive manufacturing: physical characteristics, defects, challenges and applications

Mater. Today, 49 (2021), pp. 271-295

View PDFView articleView in ScopusGoogle Scholar

[2]

S.H. Li, P. Kumar, S. Chandra, U. Ramamurty

Directed energy deposition of metals: processing, microstructures, and mechanical properties

Int. Mater. Rev. (2022), pp. 1-43

View in ScopusGoogle Scholar

[3]

N.A. Kistler, D.J. Corbin, A.R. Nassar, E.W. Reutzel, A.M. Beese

Effect of processing conditions on the microstructure, porosity, and mechanical properties of Ti-6Al-4V repair fabricated by directed energy deposition

J. Mater. Process. Technol., 264 (2019), pp. 172-181

View PDFView articleView in ScopusGoogle Scholar

[4]

T.D. Ngo, A. Kashani, G. Imbalzano, K.T.Q. Nguyen, D. Hui

Additive manufacturing (3D printing): a review of materials, methods, applications and challenges

Compos. B Eng., 143 (2018), pp. 172-196

View PDFView articleView in ScopusGoogle Scholar

[5]

E. Tan Zhi'En, J.H.L. Pang, J. Kaminski

Directed energy deposition build process control effects on microstructure and tensile failure behaviour

J. Mater. Process. Technol., 294 (2021), Article 117139

View PDFView articleView in ScopusGoogle Scholar
[6]

J. Shao, G. Yu, X. He, S. Li, Z. Li, X. Wang

Process maps and optimal processing windows based on three-dimensional morphological characteristics in laser directed energy deposition of Ni-based alloy

Opt Laser. Technol., 142 (2021), Article 107162

View PDFView articleView in ScopusGoogle Scholar
[7]

D.R. Waryoba, J.S. Keist, C. Ranger, T.A. Palmer

Microtexture in additively manufactured Ti-6Al-4V fabricated using directed energy deposition

Mater. Sci. Eng., A, 734 (2018), pp. 149-163

View PDFView articleView in ScopusGoogle Scholar
[8]

P. Kiani, A.D. Dupuy, K. Ma, J.M. Schoenung

Directed energy deposition of AlSi10Mg: single track nonscalability and bulk properties

Mater. Des., 194 (2020), Article 108847

View PDFView articleView in ScopusGoogle Scholar
[9]

C. Tan, K. Zhou, W. Ma, P. Zhang, M. Liu, T. Kuang

Microstructural evolution, nanoprecipitation behavior and mechanical properties of selective laser melted high-performance grade 300 maraging steel

Mater. Des., 134 (2017), pp. 23-34

View PDFView articleView in ScopusGoogle Scholar
[10]

O.S. Odebiyi, S.M. Adedayo, L.A. Tunji, M.O. Onuorah

A review of weldability of carbon steel in arc-based welding processes

Cogent Engineering, 6 (1) (2019), Article 1609180

View in ScopusGoogle Scholar
[11]

T. Allam, K.G. Pradeep, P. Köhnen, A. Marshal, J.H. Schleifenbaum, C. H aase

Tailoring the nanostructure of laser powder bed fusion additively manufactured maraging steel

Addit. Manuf., 36 (2020), Article 101561

View PDFView articleView in ScopusGoogle Scholar
[12]

F. Deirmina, P.A. Davies, R. Casati

Effects of powder atomization route and post-processing thermal treatments on the mechanical properties and fatigue resistance of additively manufactured 18Ni300 maraging steel

Adv. Eng. Mater. (2021), Article 2101011

Google Scholar
[13]

P. Kürnsteiner, M.B. Wilms, A. Weisheit, B. Gault, E.A. Jägle, D. Raabe

High-strength Damascus steel by additive manufacturing

Nature, 582 (7813) (2020), pp. 515-519

CrossrefView in ScopusGoogle Scholar
[14]

Y. Bai, Y. Yang, D. Wang, M. Zhang

Influence mechanism of parameters process and mechanical properties evolution mechanism of maraging steel 300 by selective laser melting

Mater. Sci. Eng., A, 703 (2017), pp. 116-123

View PDFView articleView in ScopusGoogle Scholar
[15]

S. Shamsdini, S. Shakerin, A. Hadadzadeh, B.S. Amirkhiz, M. Mohammadi

A trade-off between powder layer thickness and mechanical properties in additively manufactured maraging steels

Mater. Sci. Eng., A, 776 (2020), Article 139041

View PDFView articleView in ScopusGoogle Scholar
[16]

C. Turk, H. Zunko, C. Aumayr, H. Leitner, M. Kapp

Advances in maraging steels for additive manufacturing

BHM Berg- Hüttenmännische Monatsh., 164 (3) (2019), pp. 112-116

CrossrefGoogle Scholar
[17]

T.H. Becker, P. Kumar, U. Ramamurty

Fracture and fatigue in additively manufactured metals

Acta Mater., 219 (2021), Article 117240

View PDFView articleView in ScopusGoogle Scholar
[18]

N. Haghdadi, C. Ledermueller, H. Chen, Z. Chen, Q. Liu, X. Li, G. Rohrer, X. Liao, S. Ringer, S. Primig

Evolution of microstructure and mechanical properties in 2205 duplex stainless steels during additive manufacturing and heat treatment

Mater. Sci. Eng., A, 835 (2022), Article 142695

View PDFView articleView in ScopusGoogle Scholar

[19]

X.D. Nong, X.L. Zhou

Effect of scanning strategy on the microstructure, texture, and mechanical properties of 15-5PH stainless steel processed by selective laser melting

Mater. Char., 174 (2021), Article 111012

View PDFView articleView in ScopusGoogle Scholar
[20]

Voestalpine BÖHLER Edelstahl GmbH and Co KG

BÖHLER M789 AMPO Product Data Sheet

(2018)

Google Scholar
[21]

J. Suryawanshi, K.G. Prashanth, U. Ramamurty

Tensile, fracture, and fatigue crack growth properties of a 3D printed maraging steel through selective laser melting

J. Alloys Compd., 725 (2017), pp. 355-364

View PDFView articleView in ScopusGoogle Scholar
[22]

M.J. Paul, Y. Muniandy, J.J. Kruzic, U. Ramamurty, B. Gludovatz

Effect of heat treatment on the strength and fracture resistance of a laser powder bed fusion-processed 18Ni-300 maraging steel

Mater. Sci. Eng., A, 844 (2022), Article 143167

View PDFView articleView in ScopusGoogle Scholar
[23]

J. Mutua, S. Nakata, T. Onda, Z.-C. Chen

Optimization of selective laser melting parameters and influence of post heat treatment on microstructure and mechanical properties of maraging steel

Mater. Des., 139 (2018), pp. 486-497

View PDFView articleView in ScopusGoogle Scholar
[24]

N. Takata, R. Nishida, A. Suzuki, M. Kobashi, M. Kato

Crystallographic features of microstructure in maraging steel fabricated by selective laser melting

Metals, 8 (6) (2018)

Google Scholar
[25]

Y. Bai, D. Wang, Y. Yang, H. Wang

Effect of heat treatment on the microstructure and mechanical properties of maraging steel by selective laser melting

Mater. Sci. Eng., A, 760 (2019), pp. 105-117

View PDFView articleView in ScopusGoogle Scholar
[26]

E.A. Jägle, Z. Sheng, P. Kürnsteiner, S. Ocylok, A. Weisheit, D. Raabe

Comparison of maraging steel micro- and nanostructure produced conventionally and by laser additive manufacturing

Materials, 10 (1) (2017)

Google Scholar
[27]

J. Nguejio, F. Szmytka, S. Hallais, A. Tanguy, S. Nardone, M. Godino Martinez

Comparison of microstructure features and mechanical properties for additive manufactured and wrought nickel alloys 625

Mater. Sci. Eng., A, 764 (2019), Article 138214

View PDFView articleView in ScopusGoogle Scholar
[28]

Y. Tian, R. Palad, C. Aranas

Microstructural evolution and mechanical properties of a newly designed steel fabricated by laser powder bed fusion

Addit. Manuf., 36 (2020), Article 101495

View PDFView articleView in ScopusGoogle Scholar
[29]

C.A. Schneider, W.S. Rasband, K.W. Eliceiri

NIH Image to ImageJ: 25 years of image analysis

Nat. Methods, 9 (7) (2012), pp. 671-675

CrossrefView in ScopusGoogle Scholar
[30]

F. Niessen, T. Nyyssonen, A.A. Gazder, R. Hielscher

Parent grain reconstruction from partially or fully transformed microstructures in MTEX

J. Appl. Crystallogr., 55 (1) (2022), pp. 180-194

CrossrefView in ScopusGoogle Scholar
[31]

M. Ansari, A. Mohamadizadeh, Y. Huang, V. Paserin, E. Toyserkani

Laser directed energy deposition of water-atomized iron powder: process optimization and microstructure of single-tracks

Opt Laser. Technol., 112 (2019), pp. 485-493

View PDFView articleView in ScopusGoogle Scholar
[32]

H. Siva Prasad, F. Brueckner, A.F.H. Kaplan

Powder incorporation and spatter formation in high deposition rate blown powder directed energy deposition

Addit. Manuf., 35 (2020), Article 101413

View PDFView articleView in ScopusGoogle Scholar
[33]

H. Kitahara, R. Ueji, N. Tsuji, Y. Minamino

Crystallographic features of lath martensite in low-carbon steel

Acta Mater., 54 (5) (2006), pp. 1279-1288

View PDFView articleView in ScopusGoogle Scholar
[34]

X. Tan, Y. Kok, Y.J. Tan, M. Descoins, D. Mangelinck, S.B. Tor, K.F. Leon g, C.K. Chua

Graded microstructure and mechanical properties of additive manufactured Ti–6Al–4V via electron beam melting

Acta Mater., 97 (2015), pp. 1-16

View PDFView articleCrossrefView in ScopusGoogle Scholar
[35]

J. Macchi, S. Gaudez, G. Geandier, J. Teixeira, S. Denis, F. Bonnet, S.Y. P. Allain

Dislocation densities in a low-carbon steel during martensite transformation determined by in situ high energy X-Ray diffraction

Mater. Sci. Eng., A, 800 (2021), Article 140249

View PDFView articleView in ScopusGoogle Scholar
[36]

K. Stiller, F. Danoix, M. Hättestrand

Mo precipitation in a 12Cr–9Ni–4Mo–2Cu maraging steel

Mater. Sci. Eng., A, 250 (1) (1998), pp. 22-26

View PDFView articleView in ScopusGoogle Scholar
[37]

Y. Tian, R. Palad, L. Jiang, T. Dorin, K. Chadha, C. Aranas

The effect of heat treatments on mechanical properties of M789 steel fabricated by laser powder bed fusion

J. Alloys Compd., 885 (2021), Article 161033

View PDFView articleView in ScopusGoogle Scholar
[38]

B. Guo, Q. Zhang, L. Chen, X. Guo, N. Li, X. Liu, M. Jin

Influence of annealing temperature on the strain-hardening behavior of a lean duplex stainless steel

Mater. Sci. Eng., A, 722 (2018), pp. 216-224

View PDFView articleView in ScopusGoogle Scholar
[39]

Y. Yao, K. Wang, X. Wang, L. Li, W. Cai, S. Kelly, N. Esparragoza, M. Ros ser, F. Yan

Microstructural heterogeneity and mechanical anisotropy of 18Ni-330 maraging steel fabricated by selective laser melting: the effect of build orientation and height

J. Mater. Res., 35 (15) (2020), pp. 2065-2076

CrossrefView in ScopusGoogle Scholar
[40]

S. Shamsdini, S. Shakerin, A. Hadadzadeh, B.S. Amirkhiz, M. Mohammad i

A trade-off between powder layer thickness and mechanical properties in additively manufactured maraging steels

Mater. Sci. Eng., A, 776 (2020), Article 139041

View PDFView articleView in ScopusGoogle Scholar
[41]

Y. Yao, Y. Huang, B. Chen, C. Tan, Y. Su, J. Feng

Influence of processing parameters and heat treatment on the mechanical properties of 18Ni300 manufactured by laser based directed energy deposition

Opt Laser. Technol., 105 (2018), pp. 171-179

View PDFView articleView in ScopusGoogle Scholar
[42]

B. Li, C. Han, C.W.J. Lim, K. Zhou

Interface formation and deformation behaviors of an additively manufactured nickel-aluminum-bronze/15-5 PH multimaterial via laser-powder directed energy deposition

Mater. Sci. Eng., A, 829 (2022), Article 142101

View PDFView articleView in ScopusGoogle Scholar
[43]

C. Nyby, X. Guo, J.E. Saal, S.-
C. Chien, A.Y. Gerard, H. Ke, T. Li, P. Lu, C. Oberdorfer, S. Sahu, S. Li, C
.D. Taylor, W. Windl, J.R. Scully, G.S. Frankel

Electrochemical metrics for corrosion resistant alloys

Sci. Data, 8 (1) (2021), p. 58

View in ScopusGoogle Scholar
[44]

J. Suryawanshi, T. Baskaran, O. Prakash, S.B. Arya, U. Ramamurty

On the corrosion resistance of some selective laser melted alloys

Materialia, 3 (2018), pp. 153-161

View PDFView articleView in ScopusGoogle Scholar
[45]

L. Wang, C. Dong, C. Man, D. Kong, K. Xiao, X. Li

Enhancing the corrosion resistance of selective laser melted 15-5PH martensite stainless steel via heat treatment

Corrosion Sci., 166 (2020), Article 108427

View PDFView articleView in ScopusGoogle Scholar
[46]

C. Tan, K. Zhou, M. Kuang, W. Ma, T. Kuang

Microstructural characterization and properties of selective laser melted maraging steel with different build directions

Sci. Technol. Adv. Mater., 19 (1) (2018), pp. 746-758

CrossrefView in ScopusGoogle Scholar
[47]

Z. Wang, T.A. Palmer, A.M. Beese

Effect of processing parameters on microstructure and tensile properties of austenitic stainless steel 304L made by directed energy deposition additive manufacturing

Acta Mater., 110 (2016), pp. 226-235

View PDFView articleView in ScopusGoogle Scholar
[48]

P. Bajaj, A. Hariharan, A. Kini, P. Kürnsteiner, D. Raabe, E.A. Jägle

Steels in additive manufacturing: a review of their microstructure and properties

Mater. Sci. Eng., A, 772 (2020), Article 138633

View PDFView articleView in ScopusGoogle Scholar
[49]

C. Celada-Casero, J. Sietsma, M.J. Santofimia

The role of the austenite grain size in the martensitic transformation in low carbon steels

Mater. Des., 167 (2019), Article 107625

View PDFView articleView in ScopusGoogle Scholar
[50]

Z. Brytan, M. Król, M. Benedyk, W. Pakieła, T. Tański, M.J. Dagnaw, P. S nopiński, M. Pagáč, A. Czech

Microstructural and mechanical properties of novel Co-free maraging steel M789 prepared by additive manufacturing

Materials, 15 (5) (2022), p. 1734

View at publisherCrossrefView in ScopusGoogle Scholar
[51]

S. Amirabdollahian, F. Deirmina, L. Harris, R. Siriki, M. Pellizzari, P. Boset ti, A. Molinari

Towards controlling intrinsic heat treatment of maraging steel during laser directed energy deposition

Scripta Mater., 201 (2021), Article 113973

View PDFView articleView in ScopusGoogle Scholar
[52]

H.J. Rack

Age hardening-grain size relationships in 18Ni maraging steels

Mater. Sci. Eng., 34 (3) (1978), pp. 263-270

View PDFView articleView in ScopusGoogle Scholar
[53]

Y. Wang, L. Luo, T. Liu, B. Wang, L. Luo, J. Zhao, L. Wang, Y. Su, J. Guo, H. Fu

Tuning process parameters to optimize microstructure and mechanical properties of novel maraging steel fabricated by selective laser melting

Mater. Sci. Eng., A, 823 (2021), Article 141740

View PDFView articleView in ScopusGoogle Scholar
[54]

C.L. Li, Q.S. Mei, J.Y. Li, F. Chen, Y. Ma, X.M. Mei

Hall-Petch relations and strengthening of Al-ZnO composites in view of grain size relative to interparticle spacing

Scripta Mater., 153 (2018), pp. 27-30

View PDFView articleView in ScopusGoogle Scholar
[55]

L. Liu, J. Zhang, C. Ai

Nickel-based superalloys

F.G. Caballero (Ed.), Encyclopedia of Materials: Metals and Alloys, Elsevier, Oxford (2022), pp. 294-304

View PDFView articleView in ScopusGoogle Scholar
[56]

E.I. Galindo-Nava, P.E.J. Rivera-Díaz-del-Castillo

Understanding the factors controlling the hardness in martensitic steels

Scripta Mater., 110 (2016), pp. 96-100

View PDFView articleView in ScopusGoogle Scholar
[57]

A. Hadadzadeh, A. Shahriari, B.S. Amirkhiz, J. Li, M. Mohammadi

Additive manufacturing of an Fe–Cr–Ni–Al maraging stainless steel: microstructure evolution, heat treatment, and strengthening mechanisms

Mater. Sci. Eng., A, 787 (2020), Article 139470

View PDFView articleView in ScopusGoogle Scholar
[58]

J. Pešička, R. Kužel, A. Dronhofer, G. Eggeler

The evolution of dislocation density during heat treatment and creep of tempered martensite ferritic steels

Acta Mater., 51 (16) (2003), pp. 4847-4862

View PDFView articleView in ScopusGoogle Scholar
[59]

C. Tan, Y. Chew, F. Weng, S. Sui, Z. Du, F.L. Ng, G. Bi

Superior strength-ductility in laser aided additive manufactured high-strength steel by combination of intrinsic tempering and heat treatment

Virtual Phys. Prototyp., 16 (4) (2021), pp. 460-480

View at publisherCrossrefView in ScopusGoogle Scholar
[60]

H. Li, Y. Liu, B. Liu, D. Wei

Synergistic enhancement of strength and ductility of cobalt-free maraging steel via nanometer-scaled microstructures

Mater. Sci. Eng., A, 842 (2022), Article 143099

View PDFView articleView in ScopusGoogle Scholar
[61]

T.F. Babuska, B.A. Krick, D.F. Susan, A.B. Kustas

Comparison of powder bed fusion and directed energy deposition for tailoring mechanical properties of traditionally brittle alloys

Manufacturing Letters, 28 (2021), pp. 30-34

View PDFView articleView in ScopusGoogle Scholar
[62]

N. Martin, A. Hor, E. Copin, P. Lours, L. Ratsifandrihana

Correlation between microstructure heterogeneity and multi-scale mechanical behavior of hybrid LPBF-DED Inconel 625

J. Mater. Process. Technol., 303 (2022), Article 117542

View PDFView articleView in ScopusGoogle Scholar
[63]

P.D. Nezhadfar, P.R. Gradl, S. Shao, N. Shamsaei

Microstructure and deformation behavior of additively manufactured 17–4 stainless steel: laser powder bed fusion vs. Laser powder directed energy deposition

JOM (J. Occup. Med.) (2021), pp. 1136-1148

Google Scholar